Available online at www.sciencedirect.com

ScienceDirect

European Journal of Mechanics B/Fluids 27 (2008) 684–706

Stability of the laminar boundary layer flow encountering a row of roughness elements: Biglobal stability approach and DNS

E. Piot [a,*], G. Casalis [a], U. Rist [b]

[a] *Département Modèles pour l'Aérodynamique et l'Energétique, ONERA, 2, av. Edouard Belin, BP 4025, 31055 Toulouse Cedex, France*
[b] *Institut für Aerodynamik und Gasdynamik, Universität Stuttgart, Pfaffenwaldring 21, D-70550 Stuttgart, Germany*

Received 30 January 2007; received in revised form 16 January 2008; accepted 18 January 2008

Abstract

The stability of the laminar boundary layer developing on a flat plate in the presence of a periodic row of roughness elements is investigated. A Direct Numerical Simulation is performed to compute the steady flow downstream of the roughness elements, which contains a pair of two counter-rotating streamwise vortices per element, which can be considered as a "pre-streaky" structure. The linear stability of this base flow is analyzed by means of the so-called "biglobal" stability approach. Three-dimensional eigenmodes are found, which are shown to be the continuation of the Tollmien–Schlichting waves present in the case of an unperturbed boundary layer. Moreover, a stabilizing effect due to the roughness-induced vortices is found. A Direct Numerical Simulation of the interaction between a two-dimensional Tollmien–Schlichting wave and the roughness array is also performed. The computed perturbation traveling downstream of the roughness elements is shown to be a linear combination of the biglobal eigenmodes.

Keywords: Roughness; Laminar boundary layer; Direct Numerical Simulation; Biglobal linear stability

---

1. Introduction

The mechanisms through which laminar boundary-layer flows transition to turbulence have been studied for many years, but their understanding and further their prediction and control still remain a challenging issue for aerodynamics scientists. For certain simple configurations, such as a two-dimensional (2D), zero-pressure-gradient boundary layer, the path to turbulence in a benign disturbance environment is now well understood: a receptivity process to the disturbance environment (free-stream acoustic waves or 2D surface roughness) generates unstable spanwise-invariant Tollmien–Schlichting (TS) waves, which undergo linear exponential growth while traveling in the streamwise direction, followed by secondary instabilities, nonlinearity and finally a breakdown to turbulence. The process by which three-dimensional surface roughness affects the laminar-turbulent transition is not as well understood, and substantial recent efforts have focused on this subject. An important parameter used to assess the impact of roughness on laminar-turbulent transition is the roughness Reynolds number $Re_h = u_h \cdot h/\nu$, where u_h is the flow velocity at the roughness height h without the roughness present and ν is the kinematic viscosity of the fluid. Roughness-induced transition to

---

[*] Corresponding author.
E-mail address: estelle.piot@onera.fr (E. Piot).

0997-7546/$ – see front matter © 2008 Elsevier Masson SAS. All rights reserved.
doi:10.1016/j.euromechflu.2008.01.007

turbulence just downstream of the roughness location typically occurs when $Re_h \approx 600$ is reached [1]. Investigations of such cases have been pioneered by Acalar and Smith [2] for the experimental side, and more recently by Tufo et al. [3] and Matheis and Rothmayer [4], for the numerical side, for instance. The dominant mechanism here is vortex generation and vortex shedding, i.e., a mechanism that completely bypasses linear instability mechanisms altogether.

Smaller roughness elements are expected to have a more subtle influence, because the flow remains laminar at the perturbation and laminar-turbulent transition occurs in its wake based on mechanisms which are not yet fully understood. Roughness will enhance the receptivity of the boundary layer with respect to external disturbances, in such way that another initial spectrum of disturbances exists compared to the smooth case. It may also enhance the instability of the TS modes or even introduce new unstable modes, i.e. even the presence of subcritical roughness can alter the transition to turbulence in a boundary layer in various ways.

Many studies have investigated the flow around isolated 3D surface humps, especially with the help of asymptotical methods. For instance, the pioneering work of Bogolepov [5] gave the classification of flow around surface roughness, while Lipatov and Vinogradov [6] studied one of these flows both theoretically and numerically. The present work will rather focus on the flow generated by periodic arrays of roughness elements, which can be in some cases very different from the one around an isolated surface distortion.

1.1. *From roughness-induced vortices to streamwise streaks*

Historically, Landahl [7] found out that in shear flows disturbances in the form of streamwise vortices are very effective in transferring high-speed fluid to the low-speed fluid region while simultaneously low-speed fluid is transferred to the high-speed region. This “lift-up effect” eventually leads to large elongated spanwise modulations of the streamwise velocity called streamwise streaks. These streaks undergo an algebraic growth, which is also called transient growth (see, e.g., Reshotko [8]). This mechanism is involved in “bypass transition”. Theory of optimal transient growth [9,10] has shown that the most dangerous initial perturbations consist of steady streamwise vortices.

A first direct numerical study of the flow created by an array of 3D shallow bumps was performed by Joslin and Grosch [11]. They reproduced the experimental configuration of Gaster et al. [12]. They gave a first insight into the structure of the flow downstream of the bump and showed the existence of a complex pattern of streamwise vorticity. More recently, work has focused on understanding whether streaks can be generated by 3D roughness elements, and whether the growth of the associated steady disturbances is optimal or not. Tumin and Reshotko [13,14] have developed a theoretical analysis based on the expansion of the linearized Navier–Stokes equations into the biorthogonal eigenfunction system. They showed that behind one roughness element there are counterrotating vortices that bring the high-speed fluid down into the wake region, but transient growth has not been observed in their model. Some experiments have been performed by White and coworkers [15,16] and by Fransson et al. [17]. They both considered a periodic array of roughness elements and observed downstream of each roughness element the stationary disturbances created by the streamwise vortices. These disturbances evolved far downstream into low- and high-speed streaks. They also found that these disturbances underwent suboptimal transient growth. Numerical investigations on the same configurations have been performed by Choudhari and Fischer [18,19]. They reproduced the major trends of the aforementioned experiments, and they also studied the stabilizing effect of the roughness-induced streaks on the amplification of pre-existing unsteady TS waves in the boundary layer.

1.2. *Stabilizing effect of the roughness-induced streaks*

Indeed, in parallel to the investigations on the nature of the roughness-induced disturbances, some researchers have focused on the use of roughness elements as a passive mechanism for delaying transition to turbulence. This idea comes from the theoretical work of Cossu and Brandt [20], which shows that the presence of optimal streaks in a boundary layer induces a lower spatial growth rate of unstable TS waves. Kogan and Ustinov [21] have shown a similar effect with a spanwise-periodic stationary mass force distributed in the streamwise direction, which could increase the laminar flow interval by three to four times. Fransson et al. [22–24] have conducted wind-tunnel experiments in which they have generated stable steady streaks by means of roughness elements, as explained in the previous section, and they have shown that these streaks were effective in reducing the growth of the TS waves.

1.3. Aim of the present study

In the present study, we will focus on the close vicinity of a roughness element. In this region the process of transient growth has not yet transformed the roughness-induced vortices into the so-called streamwise streaks. The aim of this work is to investigate the stability of this strongly spanwise-varying flow (whereas the works aforementioned investigate the stability of the established streaks, which are sinusoidal in the spanwise direction). *In the following, we will use for the considered flow the denomination "pre-streaky" flow*. This stability study will be done by different methods, which will be compared and connected. A Direct Numerical Simulation will provide both the input flow for the linear stability computations, and the benchmark disturbances to be compared with the stability study results. The stability study will be performed by a biglobal[1] linear stability method. With this approach, it is possible to compute the instabilities associated to a base flow which is inhomogeneous along two spatial directions. On the contrary, the classical local stability analysis can only consider base flows inhomogeneous along a single spatial direction. The biglobal approach has been applied successfully to various physical problems. For a review, the reader may refer to the work of Theofilis [25]. A second aim of the study is then to explain how the biglobal results can be connected to the DNS ones, and what new information they can bring out.

The article is organized as follows. First the studied configuration is defined in Section 2. Then in Section 3, we describe the DNS code which is used to compute the steady base flow. In Section 4 the biglobal stability analysis is presented: both theoretical and numerical aspects are introduced. Some temporal stability results are given in Section 5. A classical local stability analysis is used to show how these results enlighten the perturbative effect of the roughness element. In Section 6 a spatial biglobal stability approach is carried out, and the roughness effect on the stability of the eigenmodes' streamwise evolution is discussed. Next, we show in Section 7 how to compare the biglobal eigenmodes to the disturbances computed by the DNS. Finally, in Section 8 the spatial stability of the pre-streaky base flow is investigated for several frequencies around the DNS one.

2. Definition of the studied configuration

In the following the coordinates x, y, and z respectively denote the streamwise, wall-normal, and spanwise directions of a flat-plate geometry subject to a x-parallel free-stream velocity U_∞ at Reynolds number $Re = U_\infty L_x/\nu = 10^5$. As represented in Fig. 1, a roughness array is placed on the flat plate, but a single roughness element will be considered for the numerical investigations, subject to spanwise periodic boundary conditions. The flow is incompressible.

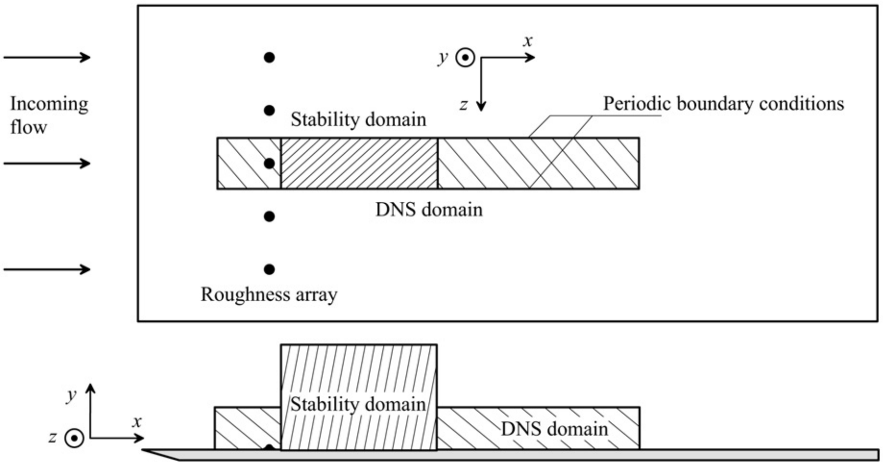

Fig. 1. Sketch of the numerical domains.

---

[1] There is no connection with the usual *global* instability. The instability mechanisms studied in this paper are purely convective.

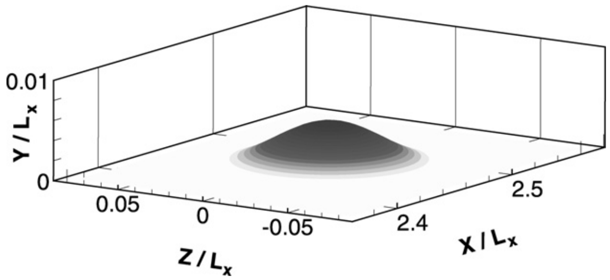

Fig. 2. Contour of a roughness element; the y-axis is stretched by a factor 5 compared to the x- and z-axes.

The roughness element is located at $x_R = 2.471L_x$, which corresponds to $Re_{\delta_1} = U_\infty \delta_1/\nu = 855$ where δ_1 is the displacement thickness of the unperturbed Blasius boundary layer. The roughness element is axisymmetric and its contour is defined by $h(x,z) = h_0 \cos^3(\pi r/d)$, with height $h_0 = 0.5\delta_1$, radial coordinate r, and diameter $d = 16.84\delta_1$ (see Fig. 2). The corresponding roughness-height Reynolds number is $Re_h = 121$. The spanwise extent of the computational domain (i.e. the spacing between the roughness elements) is $\Delta z = 3.75d = 63.165\delta_1$. The wall-normal size of the computational domain is $10.5\delta_1$ in the direct numerical simulations and $73\delta_1$ in the stability analysis.

In the following study a DNS will be performed to compute the steady flow in the DNS domain, and a second DNS will compute the perturbation generated by the interaction of an unsteady two-dimensional TS-wave with the roughness. For this, a "disturbance strip" was placed upstream of the roughness element at $x = 1.79L_x$ where wall normal suction and blowing was applied according to [26] with an amplitude of $A = 10^{-4}U_\infty$ (maximum value in the wall-normal direction of the streamwise disturbance) and a circular frequency of $\omega = 7.91U_\infty/L_x$. The inflow boundary of the integration domain is located at $x = 1.385L_x$. The streamwise coordinates of the beginning and the end of the disturbance strip are $x_1 = 1.655L_x$ and $x_2 = 1.925L_x$, respectively. The streamwise length of the disturbance strip corresponds thus to one wave length of the corresponding Tollmien–Schlichting wave ($\lambda_{\mathrm{TS}} = 0.27L_x$). The computations with periodic forcing have been performed twice with identical parameters, one time for the base flow without roughness element and one time for the base flow including the roughness elements. Thus, the influence of the roughness on the growth of the Tollmien–Schlichting wave could be assessed by an analysis of the difference between these two simulations. The linear stability of the steady DNS flow with roughness elements will also be investigated here and the results will be compared to the unsteady DNS-computed perturbation.

3. Steady flow in the vicinity of a surface nonuniformity

3.1. DNS method

For the present DNS the vorticity-velocity formulation of Rist and Fasel [26] has been extended by volume-force terms $\vec{F} = (F_x, F_y, F_z)$ such that the three vorticity-transport equations now read as

$$\begin{aligned}
&\frac{\partial \omega_x}{\partial t} + \frac{\partial}{\partial y}(v\cdot\omega_x - u\cdot\omega_y) - \frac{\partial}{\partial z}(u\cdot\omega_z - w\cdot\omega_x) = \frac{1}{Re}\left(\frac{\partial^2\omega_x}{\partial x^2} + \frac{\partial^2\omega_x}{\partial y^2} + \frac{\partial^2\omega_x}{\partial z^2}\right) + \frac{\partial F_y}{\partial z} - \frac{\partial F_z}{\partial y},\\
&\frac{\partial \omega_y}{\partial t} - \frac{\partial}{\partial x}(v\cdot\omega_x - u\cdot\omega_y) + \frac{\partial}{\partial z}(w\cdot\omega_y - v\cdot\omega_z) = \frac{1}{Re}\left(\frac{\partial^2\omega_y}{\partial x^2} + \frac{\partial^2\omega_y}{\partial y^2} + \frac{\partial^2\omega_y}{\partial z^2}\right) + \frac{\partial F_z}{\partial x} - \frac{\partial F_x}{\partial z},\\
&\frac{\partial \omega_z}{\partial t} + \frac{\partial}{\partial x}(u\cdot\omega_z - w\cdot\omega_x) - \frac{\partial}{\partial y}(w\cdot\omega_y - v\cdot\omega_z) = \frac{1}{Re}\left(\frac{\partial^2\omega_z}{\partial x^2} + \frac{\partial^2\omega_z}{\partial y^2} + \frac{\partial^2\omega_z}{\partial z^2}\right) + \frac{\partial F_x}{\partial y} - \frac{\partial F_y}{\partial x}.
\end{aligned} \tag{1}$$

According to Peskin [27] such an approach allows the simulation of arbitrary body shapes on a Cartesian grid, because the effect of the surface irregularity on the surrounding flow field is modeled with an external force field that enforces no-slip and no-throughflow at selected grid points or at selected points between the grid points at every time step. It has already successfully been applied, for example by Goldstein et al. [28], Linnick [29] or von Terzi et al. [30]. The force terms on the right-hand side of equation 1 are written as

$$\vec{F}(\vec{x},t) = \oint \vec{f}(\vec{x}_s,t)\cdot\delta(\vec{x}-\vec{x}_s)\,dS, \tag{2}$$

where $\vec{f}(\vec{x}_s, t)$ describes discrete unsteady force terms and the integration $\oint dS$ is performed over all discrete source terms. For numerical reasons, the delta function is approximated by a Gaussian as follows

$$\delta \approx \exp\bigl\{-\bigl[(x - x_s)/\sigma_x\bigr]^2 - \bigl[(y - y_s)/\sigma_y\bigr]^2 - \bigl[(z - z_s)/\sigma_z\bigr]^2\bigr\}, \tag{3}$$

with $\sigma_x = 2\Delta x$, $\sigma_y = 2\Delta y|_{\text{wall}}$, and $\sigma_z = 2\Delta z$. The discrete surface body forces $\vec{f}$ are determined from the relation

$$\vec{f}(\vec{x}_s, t) = \alpha_s \cdot \int_0^t \vec{v}(\vec{x}_s, t')\, dt' + \beta_s \cdot \vec{v}(\vec{x}_s, t) \tag{4}$$

with negative constants α_s, β_s (cf. [27]). Eq. (4) represents a feedback-control scheme that drives the solution iteratively towards a desired surface velocity $\vec{v}(\vec{x}_s, t)$ on the surface of the irregular boundary $\vec{x}_s$. The parameters α_s and β_s should be large in order to enforce an immediate reaction of the flow field on changes of the imposed surface. However, numerical instability results if they are chosen too large. If the surface of the boundary is located between grid points, the velocity at this location is interpolated from the values at the neighbouring grid points using a fourth-order Lagrangian interpolation procedure.

Use of the forcing terms in Eqs. (1)–(4) is restricted to the region of the roughness element. The control parameters α_s and β_s were set to $-500\,000$ and -500, respectively. With these parameters, the feedback control converged within the time advancement of the four-step Runge–Kutta scheme, such that no extra iteration appeared necessary to further iterate the body forces. The accuracy of the scheme was checked in a number of two- and three-dimensional unsteady simulations where receptivity coefficients were computed which turned out to be in excellent quantitative agreement with experimental measurements by Würz et al. [31].

Because of the spectral representation of the spanwise coordinate which is incompatible with the singularities in $\vec{F}$ a weak spectral filter had to be used in that direction to avoid spurious oscillations, as in [28], for instance. The filter was implemented by multiplying the vorticity of each spectral mode k by $e^{-(k/K)^{20}}$, where K is the highest spectral mode used for discretization. A special correction procedure for the normal-to-the-wall derivatives, as suggested in [30], was not necessary because the velocity inside the roughness was not set to zero.

The flow field is discretized using fourth-order-accurate finite differences in x and y-directions and a spectral ansatz in z to account for periodic boundary conditions in spanwise direction and inflow and outflow conditions in streamwise direction. The time integration of the three vorticity transport equations is done using a fourth-order, four-step Runge–Kutta scheme. The evaluation of the nonlinear terms in Eq. (1) is performed using a pseudo-spectral scheme according to Orszag [32]. The Poisson equation for the wall-normal velocity component v is solved with a multigrid method, using a vectorizable, stripe-pattern successive over relaxation (SOR) line-iteration technique on each of four subgrids, and the wall-parallel velocity components u and w are solved from ordinary equations (after discretization) [26]. Note that its computational effort is comparable to Davies and Carpenter "new vorticity-velocity formulation" [33] because the present method needs to compute the nonlinear terms for *two* vorticity transport equations only and solves only one full Poisson equation.

At the inflow boundary steady Blasius boundary-layer velocity and vorticity profiles are prescribed and the vorticity is set to zero at the free-stream boundary, because this boundary lies in the region of potential flow. This also leads to exponential decay for the wall-normal velocity v. Except for the small disturbance strip, where controlled fluctuations can be introduced by wall-normal periodic suction and blowing, the no-slip and no-through-flow condition is applied at the wall. Upstream of the outflow boundary, the unsteady vorticity is smoothly damped to the steady-state value in a buffer domain [34]. Consequently, the unsteady velocity components also decay exponentially in the streamwise direction and vanish at the outflow. More details concerning the numerical method can be found in [26].

To verify the numerical results grid refinement studies in all directions have been performed. Additionally, for a two-dimensional roughness element the DNS results were compared with experimental results obtained by M. Lang in the laminar water channel of IAG at Universität Stuttgart. More two-dimensional results can be found in [35]. A minimum number of $K = 80$ spectral modes (plus their complex conjugates) were necessary to confidently resolve the narrow streamwise shear regions at the spanwise edges of the perturbation. The convergence of the results with respect to grid refinements was confirmed in a run using twice as many spectral modes, but the necessary computer time to run this simulation towards a steady state was prohibitive. Because of extremely long transients even the present coarser-scale simulation results were not yet fully steady when the simulation was stopped after $t = 13.6 L_x/U_\infty$. Remaining

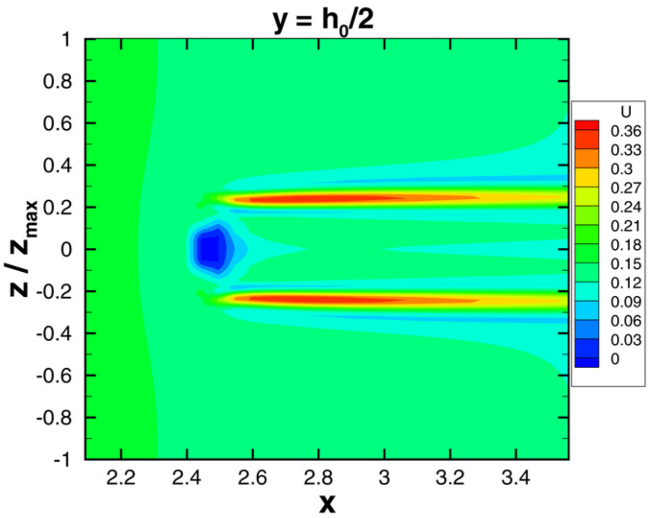

Fig. 3. Streamwise velocity at $y = h_0/2$. As $z_{\max} = \Delta z/2 = 0.27 L_x$, the z-axis is stretched by a factor 2.38 compared to the x-axis.

transients of the mean flow were filtered using high time derivatives as described in [36]. The quasi-steady results have then been used as base flow for investigations of boundary layer receptivity with respect to two-dimensional disturbances, either a plane acoustic wave or a Tollmien–Schlichting wave [37]. In the present paper, results of the latter case will be presented further down in Section 7, while the quasi-steady results will be used as a base flow for all the stability calculations.

3.2. *Base flow used for the stability calculations*

3.2.1. *Presentation of the base flow configuration*

In the following study all the variables are dimensionless. The velocity components are scaled by the free-stream velocity U_∞. The length scale L_x in the streamwise direction differs from the length scale L used for the wall-normal and spanwise directions: $L_x/L = \sqrt{10^5}$. The DNS-computed steady streamwise velocity is plotted in Figs. 3 and 5. The other velocity components $(\bar{V}, \bar{W})$ (associated with (y, z)) are small compared to $\bar{U}$ (of order 10^{-3}), but will not be neglected yet. Indeed, they reach their largest values and gradients in regions where $\bar{U}$ is relatively small. The three-dimensional structure of the flow field can be inferred from the results presented in Figs. 4 and 5. It should be noted that these figures are stretched by, respectively, a factor 15 and 7.5 in the y direction as compared to the z direction. Fig. 4 shows the structure of the streamwise vorticity field, which is similar to the one obtained by Joslin and Grosch [11]. A pair of counter-rotating vortices is developing on each spanwise side of the roughness. Between the vortices and the wall there is a region of vorticity due to the outflow in the $\pm z$ directions. As the flow evolves downstream, the vortices lift from the wall and weaken. A close look at Fig. 4 shows that the weakening is more important for the inner vortices than for the outer ones. It must also be noted that the present vorticity levels correspond to very weak rotation rates: a fluid particle must travel a streamwise distance of several L_x to complete a full revolution. Anyway, in the middle of each pair of the vortices, high-speed fluid from the outer region of the boundary layer is transported towards the wall, whereas on the outer edge of the two vortices, low-speed fluid from the near wall region is transported away from the wall. The resulting effect is clearly visible in Fig. 5(b), which shows the difference between the streamwise velocity in the case with the roughness element and in the smooth case.

3.2.2. *Discussion*

The present flow configuration can be compared to the one observed in previous studies, especially the experiments carried out by White and Ergin [15] and by Fransson et al. [17], and the direct numerical simulations performed by Joslin and Grosch [11]. The physical characteristics of all these studies are summarized in Table 1. In all cases, the observed flow field is characterized by the formation of streamwise elongated velocity perturbations, and by the presence of streamwise vortices in the near field downstream of the roughness element. The spanwise structure of

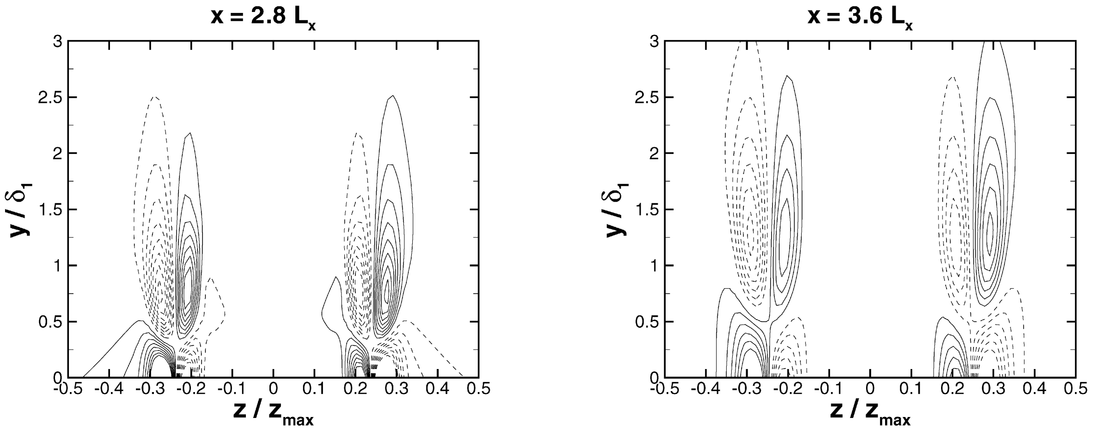

(a) The contours values are -4 to 4 in steps of 0.5, excluding 0. (b) The contours values are -1.5 to 1.5 in steps of 0.25, excluding 0.

Fig. 4. Contours of $\bar{\omega}_x$, the streamwise component of the base flow vorticity, made dimensionless by U_∞ and L_x. Contours with positive values of $\bar{\omega}_x$ are solid and those with negative values are dashed. Positive $\bar{\omega}_x$ indicates counterclockwise rotation and negative clockwise.

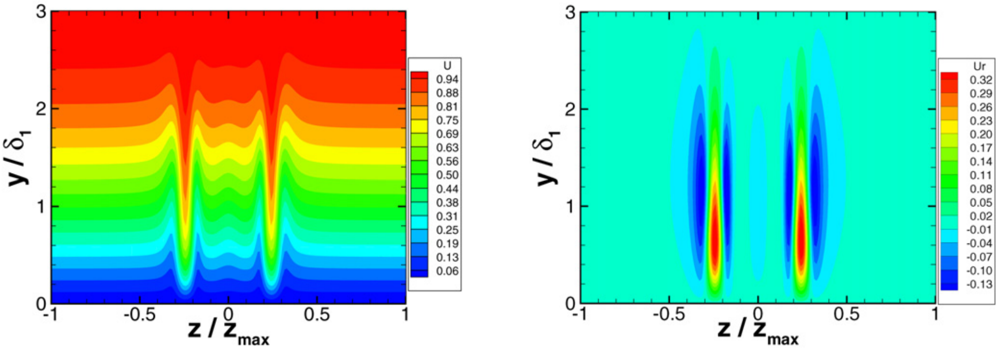

(a) $\bar{U}(y,z)$ (b) $\bar{U}(y,z) - \bar{U}(y, z_{\max})$

Fig. 5. Streamwise velocity at $x = 3L_x$. Right-hand side figure shows the difference between the case with the roughness element and the case without roughness, which corresponds to a two-dimensional Blasius boundary layer flow.

Table 1

Comparison of the physical characteristics of the studied configuration with those of previous studies. δ_1 is the displacement thickness of the undisturbed boundary layer at the roughness location. h, l_x and l_z stand for the height, the streamwise and the spanwise extent of the roughness element, respectively. λ_z is the spanwise spacing between the elements

	Roughness shape	h/δ_1	l_x/δ_1	l_z/δ_1	λ_z/δ_1	Re_h	Re_{δ_1}
Present study	$\cos^3\left(\frac{\pi\sqrt{x^2+z^2}}{l_x}\right)$	0.5	16.84	16.84	63	121	855
White and Ergin [15]	cylinder	0.57	6.35	6.35	19	119	677
Fransson et al. [17]	cylinder	1.44	3.7	3.7	14.8	285	253
Joslin and Grosch [11]	$\cos^3\left(\frac{\pi x}{l_x}\right)\cos^3\left(\frac{\pi z}{l_z}\right)$	0.1	15.9	13	50	7	1200

the flow field seems to depend on the competition between the streamwise vortices and the wake effects. Indeed, the vortices push high-speed fluid towards the wall and lift low-speed fluid on their outer sides, whereas the wake creates a velocity defect behind the roughness element. As explained by Choudhari and Fischer [19], the spanwise extent of the roughness element (i.e. the l_z/δ_1 ratio) plays a major role in determining the downstream spacing between the streamwise vortices and, hence, their effectiveness in modifying the velocity distribution along the centerline. Moreover, as pointed out by Fransson et al. [22], the strength of the vortices is related to the roughness height (more precisely to the h/δ_1 ratio); the shape of the latter is also an important parameter. Concerning the spanwise structure of the vorticity field, the linear computations by Tumin and Reshotko [13] applied to the configuration of White and

Ergin or Joslin and Grosch predict the existence of *one* pair of counterrotating streamwise vortices. Conversely, as discussed in [13], the nonlinear simulations of the same configurations, performed by Fisher and Choudhari [18] and Joslin and Grosch show a pair of *two* counterrotating streamwise vortices, similar to those observed in the present study. Tumin and Reshotko explain this discrepancy by the nonlinear character of the receptivity mechanism.

In the present case, each pair of counterrotating vortices generates one high-speed and two low-speed regions, while the wake effect creates a velocity deficit along the centerline (see Fig. 5(b)). On the contrary, previous studies presented in Table 1 show that in the near field region there is only a velocity deficit on the centerline with high-speed fluid on both sides. We believe that in the present case the spanwise distance between the vortices is so large (due to a large l_z/δ_1 ratio) that the low-speed fluid region created by the inner vortices cannot merge with the wake region, as happens in the other configurations. This effect could also be increased by the fact that the shape of the roughness element is quite flat in the present configuration.

Further downstream, experiments by White and Ergin [15] and by Fransson et al. [17] show that the flow structure evolves gradually into a classical streaky structure, i.e. into a spanwise sinusoidal modulation of the boundary layer. This evolution is strongly influenced by the proximity of the flow structures induced by other roughness elements, as clearly shown by Fig. 4 in [17]. The distance after which this process is over and where the streaks become fully established seems to depend strongly on the configuration parameters. In the present configuration, as well as in Joslin and Grosch's one, this process is not observable before a streamwise distance to the roughness location of about $100\delta_1$, which is beyond the end of the present computational domain.

In the following sections, the flow $(\bar{U}, \bar{V}, \overline{W})$ presented above will be used as the base flow for the stability calculations. This flow will be denoted as the steady "pre-streaky" flow. Indeed, as explained previously, the region studied in the present work consists of the near to intermediate wake region, in which the spanwise flow structure is still rather complicated. Further downstream, the streamwise vortices shown in Fig. 4 will decay and the pre-streaky structures will interact with that created by other elements, leading to fully established streaky flow.

4. Formulation of the biglobal linear stability analysis

4.1. Governing equations

The stability analysis of the pre-streaky flow, which will from now on be called the *base flow*, is performed under the standard simplifying approximation of a "parallel flow", i.e. it is assumed to evolve slowly in the streamwise direction. It is therefore justified to analyze the local stability of the pre-streaky flow by considering, at each streamwise location X, the parallel flow obtained by "freezing" the local velocity profiles $(\bar{U}(X,y,z), \bar{V}(X,y,z), \overline{W}(X,y,z))$ and neglecting their streamwise gradients. In this context, X must be considered as a parameter and not as the current streamwise coordinate x. Some small perturbation velocity components $(\hat{u}, \hat{v}, \hat{w})$ and pressure $\hat{p}$ are superimposed to the base flow, and we then proceed to linearize the incompressible Navier–Stokes equations about the base flow. The linearized equations read:

$$\begin{cases} \hat{u}_x + \hat{v}_y + \hat{w}_z = 0, \\ \hat{u}_t + \bar{U}\hat{u}_x + \bar{U}_y\hat{v} + \bar{U}_z\hat{w} + \bar{V}\hat{u}_y + \overline{W}\hat{u}_z + \hat{p}_x = \frac{1}{R}\nabla^2\hat{u}, \\ \hat{v}_t + \bar{U}\hat{v}_x + \bar{V}_y\hat{v} + \bar{V}_z\hat{w} + \bar{V}\hat{v}_y + \overline{W}\hat{v}_z + \hat{p}_y = \frac{1}{R}\nabla^2\hat{v}, \\ \hat{w}_t + \bar{U}\hat{w}_x + \overline{W}_y\hat{v} + \overline{W}_z\hat{w} + \bar{V}\hat{w}_y + \overline{W}\hat{w}_z + \hat{p}_z = \frac{1}{R}\nabla^2\hat{w} \end{cases} \tag{5}$$

where ∇^2 stands for the Cartesian Laplacian, $\hat{q}_a = \partial\hat{q}/\partial a$ and R is the Reynolds number based on the length scale L. Indeed, it has to be pointed out that the current streamwise coordinate x and the associated derivatives are rescaled with L, whereas the frozen parameter X is rescaled with L_x. The velocities are, as for the DNS, scaled by the freestream velocity.

As the base flow is steady and frozen in the streamwise direction, solutions of (5) can be sought in the form of normal modes:

$$\hat{q}(x,y,z,t) = q(y,z)\exp \mathrm{i}(\alpha x - \omega t) \tag{6}$$

where q stands for any perturbation field, α is the streamwise wavenumber, ω is the circular frequency and $\mathrm{i} = \sqrt{-1}$. Both α and ω can be complex numbers, depending on the type of stability which is studied: if α is complex, it is a spatial stability, while if ω is complex, it is a temporal stability. When introducing the form (6) into the system (5), a second-order partial differential equation (PDE) in y and z is obtained, whose coefficients depend on the base flow, on α and ω, and on the Reynolds number R:

$$\mathcal{L}\{\bar{U}, \bar{V}, \overline{W}, \alpha, \omega, R\}(u, v, w, p) = 0. \tag{7}$$

This equation can be recast in a standard generalized eigenvalue problem:

- either

$$\mathcal{A}Q = \omega\mathcal{B}Q \tag{8}$$

  with ω the complex eigenvalue and $Q = [u, v, w, p]$ the eigenfunction vector
- or

$$\mathcal{A}'Q' = \alpha\mathcal{B}'Q' \tag{9}$$

  with α the complex eigenvalue and $Q' = [Q, \alpha Q]$ the eigenfunction vector, Q still standing for $[u, v, w, p]$.

We shall consider the perturbations with a spanwise period coinciding with the period of the base flow. It is not a common case, but only such disturbances are generated when 2D TS wave interacts with the roughness. For this case, Eq. (7) has some symmetry properties which lead to a reduction of the problem. Indeed $\bar{U}$ and $\bar{V}$ are symmetric about $z = 0$, while $\overline{W}$ is antisymmetric. A mathematical analysis shows that if all eigenvalues are simple eigenvalues, the eigenfunctions have necessarily either an odd or an even z-symmetry. More precisely, two combinations are possible:

- u, v, p are symmetric about $z = 0$ and w is antisymmetric; in the following sections, this case will be named as the "*even v*" case (in the literature these eigenmodes are often called "varicose");
- u, v, p are antisymmetric about $z = 0$ and w is symmetric; in the following sections, this case will be named as the "*odd v*" case (these modes are usually called "sinuous");

The size of system (7) can then be reduced by considering only half of the spanwise domain, for instance $z \in [0, z_{\max}]$, and by using the previous symmetry properties.

Homogeneous Dirichlet boundary conditions on u, v and w are enforced at the plate ($y = 0$) and in the free stream. For the pressure a homogeneous Dirichlet condition is used in the free stream and a compatibility condition at the wall. In the spanwise direction, a combination of periodicity and parity conditions are used. Therefore homogeneous boundary conditions hold at $z = 0$ and $z = z_{\max}$ for w, u_z, v_z and p_z in the "even v" case, and for u, v, p and w_z in the "odd v" case.

4.2. Numerical procedure

The problem presented in the previous section is called a *biglobal stability analysis*, because no specific assumption is made on the (y, z)-mathematical dependence of the perturbations. System (7) is discretized in each direction with Chebyshev expansions evaluated at the Gauss–Lobatto collocation points [38]. The z-domain is split into two subdomains, and mapped through homothetic transformations to $[0, L_c]$ and $[L_c, L_z]$, in order to get a refined grid in the region of the streaks. N_y points are used in the wall-normal direction, N_z points in the spanwise direction. The DNS base flow and the associated spatial gradients are interpolated on the stability grid.

The PDE written as the temporal eigenvalue problem (8) corresponds thus to a matrix which is $4 \cdot N_y \cdot N_z$ large, whereas in the case of the spatial eigenvalue problem (9), the matrix is twice as large. Because of memory size limitations of our available computing system, only the temporal eigenvalue problem can be solved; this is done with an Arnoldi method. For a fixed real value of α, complex eigenvalues ω and the associated eigenvectors are computed. As shown in Fig. 6, the results are considered converged for $(N_y, N_z) = (41, 60)$, at least for the most amplified modes. This number of points will be used in all the following computations. In Fig. 6 four modes are represented: two of them are temporally unstable ($\omega_i > 0$), another one is marginally stable ($\omega_i \approx 0$), the last one is stable.

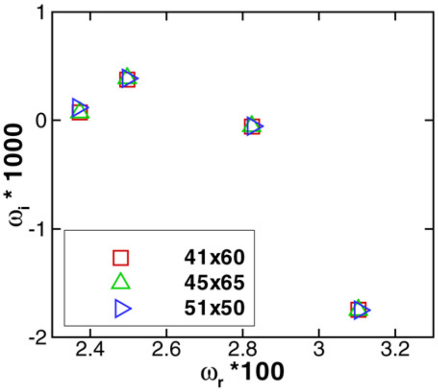

Fig. 6. Temporal eigenvalues for $X = 3$ and $\alpha = 7.03 \times 10^{-2}$. "Even v" case. The values of $N_y \times N_z$ are given in the legend.

5. From biglobal to local stability analysis

To understand what represent the results obtained by the biglobal stability analysis, and why this method is useful for the studied problem, let us consider some usual local stability methods.

In the following section, all the computations will be performed for a fixed streamwise position $X = 3$.

5.1. Floquet theory

As the base flow is z-periodic, Floquet theory can be used. This is the method used by Cossu and Brandt [20] for their stability study on the optimal streaks. In their case the base flow was thus not only periodic in the spanwise direction, but also sinusoidal in this direction. Following the Floquet theory, the perturbation admits the following expansion:

$$q(y,z) = q_0(y,z)\mathrm{e}^{\mathrm{i}\gamma\beta z} = \mathrm{e}^{\mathrm{i}\gamma\beta z}\sum_{k=-m}^{m} q_k(y)\mathrm{e}^{\mathrm{i}k\beta z} \tag{10}$$

where the amplitude q_0 has the same spanwise periodicity as the base flow, γ is the detuning parameter defined in the range $|\gamma| \leqslant 1/2$ and $\beta = \pi/z_{\max}$ is the spanwise wavenumber corresponding to the base flow periodicity. A similar Fourier decomposition is used for the base flow, which is then substituted, as well as (10), in (7). By collecting terms with like powers of $\mathrm{e}^{\mathrm{i}k\beta z}$, the PDE reduces to a set of ordinary differential equations. Unfortunately, as the base flow evolves very strongly in the spanwise direction (contrary to what happens in the case of an optimal streak), about 50 terms are needed to get a correct Fourier decomposition. Moreover, as the biglobal stability results show that the z-evolution of the perturbations presents sharp peaks, a very high number of terms will also be needed in (10) to obtain converged results. Finally, the size of the matrix obtained after discretization of the set of ordinary differential equations will be prohibitive for numerical calculations, even if this matrix is sparse. The Floquet method is therefore unusable on this problem, and does not provide any improvement with respect to the biglobal analysis.

5.2. Small perturbation method

The base flow is obtained by a DNS computation of the flow developing over a flat plate with a surface roughness element. We can consider that this roughness induces a modification of the classical flat plate boundary layer flow, and we can try to solve the stability problem with a perturbation method.

5.2.1. Flat plate parallel base flow

First of all, we apply the biglobal stability on a simplified form of the base flow, which is the simplified flow calculated at $z = z_{\max}$:

$$\bar{Q}_0 = \{\bar{U}_0(y) = \bar{U}(y, z_{\max});\ \bar{V}_0 = 0;\ \overline{W}_0 = 0\}. \tag{11}$$

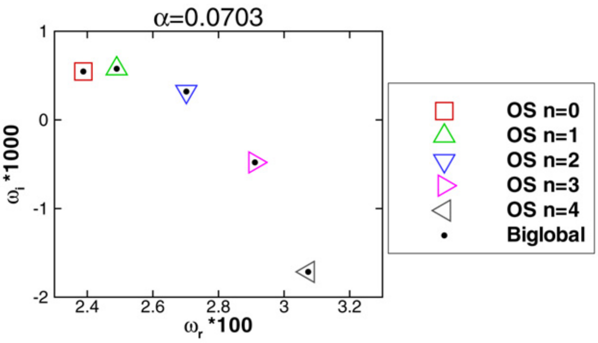

Fig. 7. Temporal eigenvalues computed by the biglobal and Orr–Sommerfeld approaches for the parallel base flow case $\bar{Q}_0$. Both results are perfectly superposed. $\alpha = 7.03 \times 10^{-2}$ and $X = 3$. “Even v” case.

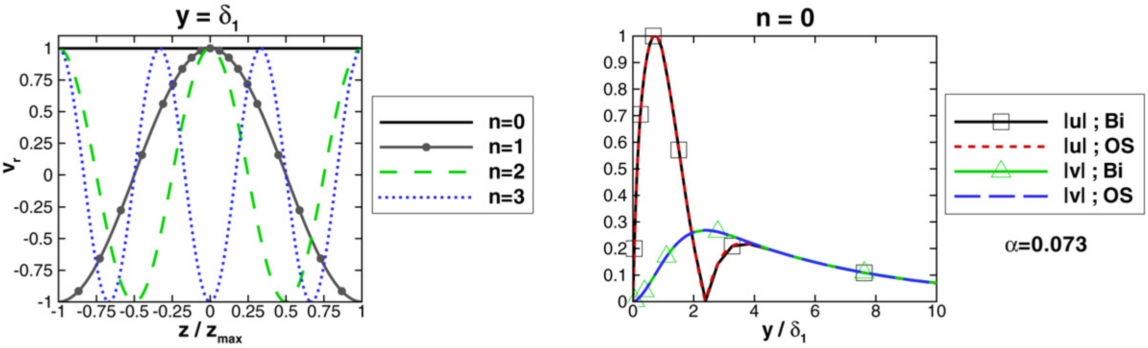

(a) Biglobal stability result for the real part of the v eigenfunction.

(b) Biglobal (Bi) and Orr–Sommerfeld (OS) results for the wall-normal evolution of the eigenfunctions. Case $n = 0$.

Fig. 8. Spatial evolution of the eigenfunctions for the parallel base flow case. $\alpha = 7.03 \times 10^{-2}$ and $X = 3$. “Even v” case. (a): spanwise evolution; (b): wall-normal evolution.

This velocity field is very similar to the boundary layer flow on a z-infinite flat plate without nonuniformities. As this base flow is invariant in the spanwise direction, the perturbations can now be sought as normal modes $q(y)\exp(\mathrm{i}n\beta z)$, where n is an integer. Here β still represents $\pi/z_{\max}$, since the studied physical configuration requires a $2z_{\max}$-spanwise periodicity. With these hypotheses, system (7) can be reduced to the classical Orr–Sommerfeld equation, which is solved for each integer value n. The computed perturbations are the famous Tollmien–Schlichting (TS) waves. The stability analysis of the base flow $\bar{Q}_0$ is thus easily solved by the Orr–Sommerfeld approach.

It is however interesting to study the stability of the parallel base flow $\bar{Q}_0$ by means of the biglobal approach, with which no specific assumptions on the z or y-dependence of the perturbations are done. This will be a way to validate the biglobal code. The results are shown in Figs. 7 and 8, for the case “even v”. Fig. 7 shows that distinct eigenvalues are obtained. When looking at the associated eigenfunctions, for instance v as plotted in Fig. 8(a), we observe that the eigenfunctions evolve as $\cos(n\beta z)$, as expected. Moreover, the calculated values of ω (see Fig. 7), as well as the y-evolution of the perturbations (see Fig. 8(b)), are the same as the ones predicted by the Orr–Sommerfeld computation. Hence the biglobal stability code provides correct results.

5.2.2. *Roughness impact on stability*

Fig. 7 shows results which are similar but different to the eigenvalues plotted in Fig. 6. To investigate the link between the parallel and the pre-streaky case, a small perturbation method is used. For this, the base flow presented in Section 3.2 is interpreted as the superposition of a roughness-induced steady flow $\bar{Q}_1$ on the parallel flow $\bar{Q}_0$ given in Eq. (11):

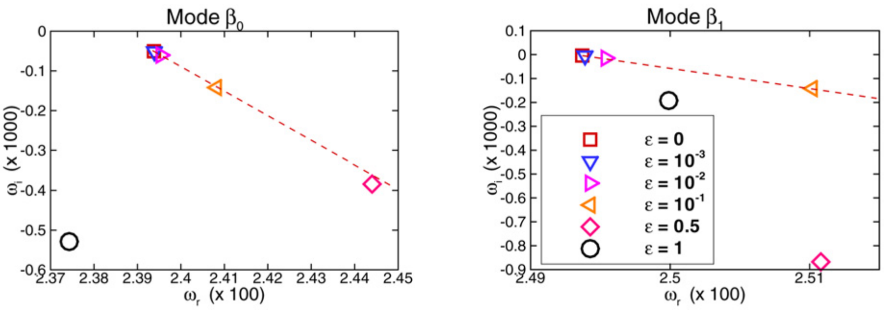

(a) (b)

Fig. 9. Eigenvalues computed by the biglobal stability method for various ε values. $\alpha = 7.03 \times 10^{-2} - 1.45 \times 10^{-3}\mathrm{i}$ and $X = 3$. "Even v" case.

$$\begin{cases} \bar{U}(y,z) = \bar{U}_0(y) + \bar{U}_1(y,z), \\ \overline{V}(y,z) = 0 + \overline{V}_1(y,z), \\ \overline{W}(y,z) = 0 + \overline{W}_1(y,z). \end{cases} \tag{12}$$

In practice $\bar{Q}_1$ is thus given by $\bar{Q}_1(y,z) = \bar{Q}_{\mathrm{DNS}}(y,z) - \bar{Q}_0(y)$. A similar decomposition is applied on the eigenvalue and on the eigenfunction vector: $\omega = \omega_0 + \omega_1$ and $Q = Q_0 + Q_1$. All the variables with a "1" subscript are assumed to be small compared to the ones with a "0" subscript. The validity of this assumption will be checked afterwards. Substituting this decomposition into 7 and separating the leading and second order terms yields two PDE:

- $\mathcal{L}_0(\bar{Q}_0, \alpha, \omega_0)Q_0 = 0$, which can be reduced to the Orr–Sommerfeld equation. Indeed, because of the spanwise invariance of $\bar{Q}_0$, a modal form in z can be used for Q_0, and the $\partial/\partial z$ terms in $\mathcal{L}_0$ leads to a multiplication by $\mathrm{i}n\beta$. An ODE is therefore obtained, and the computation of ω_0 and Q_0 is very easy.
- $\mathcal{L}_0(\bar{Q}_0, \alpha, \omega_0)Q_1 = \mathcal{L}_1(\bar{Q}_1, \alpha, \omega_1)Q_0$, which cannot be reduced to an ODE. However, thanks to the Fredholm alternative, ω_1 can be quite easily computed; the computation of Q_1 is much more complicated.

This approach is justified if the roughness-induced base flow is small compared to the parallel base flow. If not, the separation between the leading and second orders is not allowed. To check the validity of the assumption, we have introduced an artificial multiplying coefficient into the base flow decomposition: $\bar{Q}(y,z) = \bar{Q}_0(y) + \varepsilon\bar{Q}_1(y,z)$. For $\varepsilon = 0$, the base flow is parallel, for $\varepsilon = 1$, the base flow is the one presented in Section 3.2. Therefore ε quantifies the influence of the roughness on the base flow, keeping in mind that only $\varepsilon = 0$ and $\varepsilon = 1$ correspond to physically admissible solutions. Biglobal stability analysis have been performed for various values of ε. Some eigenvalues are plotted in Fig. 9. The legend is the same for both subfigures. The eigenmodes are named according to the n value which defines them in the parallel case: β_n is the mode which evolves as $\exp(\mathrm{i}n\beta z)$ in the parallel case. Fig. 9(a) corresponds to β_0, Fig. 9(b) to β_1.

Fig. 9 shows that, whatever the mode, ω depends linearly on ε as long as $\varepsilon \leqslant 0.1$ (as shown by the dashed line). The gradient is roughly equal to the ω_1 value computed by the Fredholm alternative [39]. A straight line has been plotted on the figures to visualize this dependence. Linear regressions have been performed for different modes, and give very good correlation coefficients (always above 0.9999). The "small perturbation" assumption is false as soon as $\varepsilon > 0.1$ and especially for $\varepsilon = 1$.

Fig. 10 shows the ε-evolution of the eigenfunctions associated to the β_0 and β_1 modes. All eigenfunctions have been normalized to their values at $z = z_{\max}$. The growing influence of the roughness (located at $z = 0$) is clearly visible. On the same figure is plotted the steady base flow streamwise velocity. As expected, the strong z-evolution of the stability modes occurs at the location of high spanwise gradients of the base flow.

The results presented so far confirm that the roughness has a perturbative effect on the base flow stability, but that this effect cannot be predicted by the small perturbation method for the considered flow, the roughness influence on the base flow being already too strong. Nevertheless, the approach used in this section enables us to understand that the obtained eigenmodes are a sort of "continuation" of the two-dimensional (i.e. parallel) TS-waves into three dimensional pre-streaky TS-waves (in a similar way of what is shown in Cossu and Brandt [20] and Ustinov [40]). As

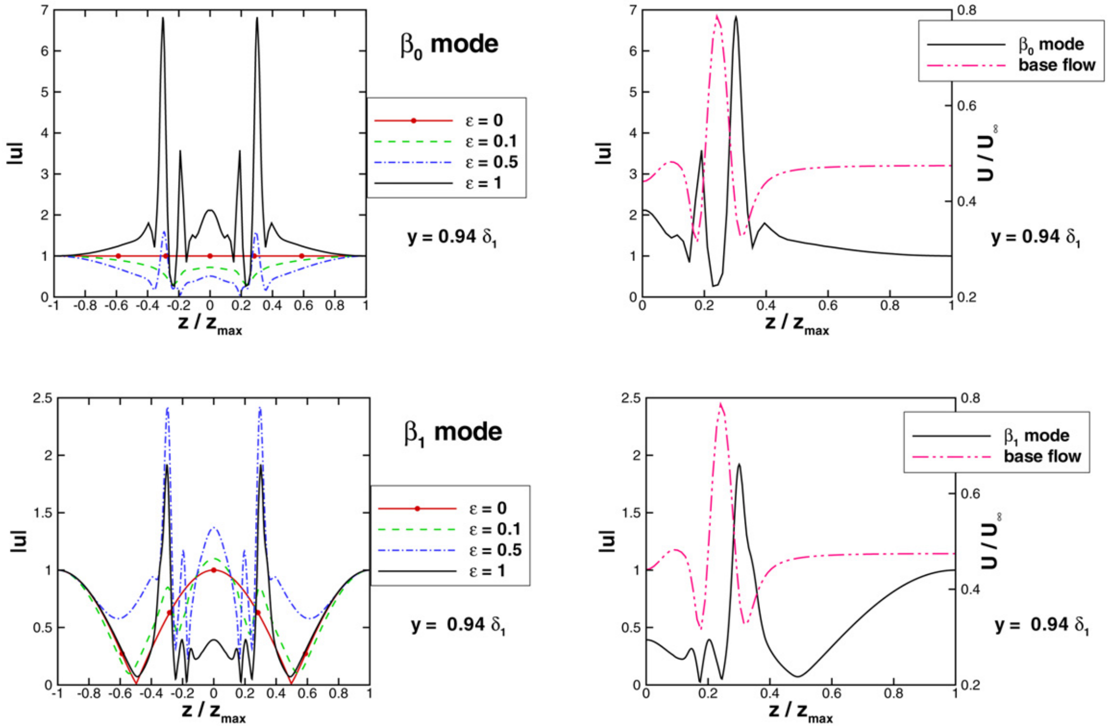

(a) stability modes for various ε values (b) stability modes for $\varepsilon = 1$ and $\bar{U}/U_\infty$

Fig. 10. Variation of ε (left-hand side figures) and comparison with the base flow (right-hand side figures). Biglobal stability results obtained for $\alpha = 7.03 \times 10^{-2} - 1.45 \times 10^{-3}\mathrm{i}$ and $X = 3$. "Even v" case.

a consequence it has been possible to label the modes thanks to the spanwise wavenumber coefficient n obtained for $\varepsilon = 0$.

6. Streamwise evolution of the perturbations

In the following section the biglobal analysis will be performed on the steady DNS pre-streaky flow (i.e. that corresponding to $\varepsilon = 1$).

6.1. Newton–Raphson method

As explained in Section 4, the spatial eigenvalue problem formulation (9) has not be solved by Arnoldi's method because the associated matrix is too large. However in the DNS simulation with a TS-wave, the obtained disturbances were oscillating at a fixed real circular frequency, and it has been observed that they were developing in the streamwise direction. In order to compare the stability results with the DNS results, it is thus necessary to solve the stability problem for a fixed real value ω and a complex wavenumber α.

This can be done by using a Newton–Raphson method applied to the PDE (7). The boundary conditions are the same as in Section 4, except at the plate, where for the "even v" case, the boundary condition $v = 0$ is replaced by the relation $v(y = 0, z) - v(0, 0)(1 - z^2/z^2_{\max}) = 0$, while for the "odd v" case it is $w = 0$ which is replaced by the relation $w(y = 0, z) - w(0, 0)(1 - z^2/z^2_{\max}) = 0$. The (system + boundary conditions) is discretized as explained in Section 4. A dishomogenization relation at the $(y = 0, z = 0)$ point is then enforced, and the Newton–Raphson iteration process is performed from a guess value of α until the convergence criterion $v(0, 0) = 0$ (or $w(0, 0) = 0$, depending on the parity case) is reached. With this method, we can compute the value of α and the associated eigenfunctions for a fixed value of ω and X, and this for each β_n mode defined previously.

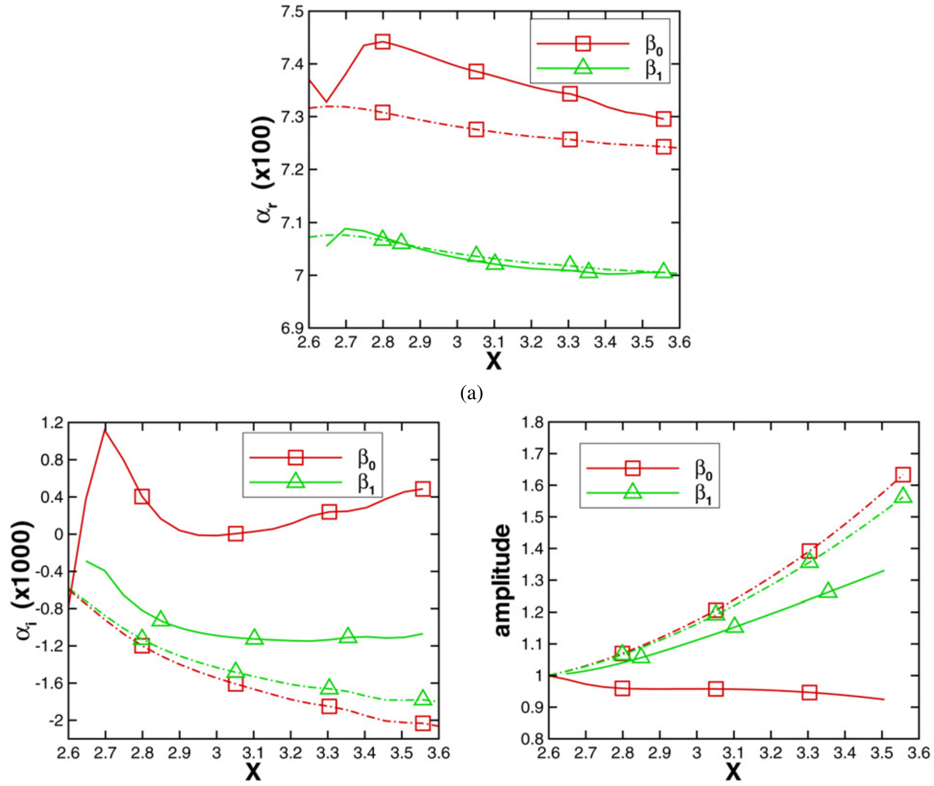

(a)

(b)

(c)

Fig. 11. Streamwise evolution of α and of the amplitude $A(X, 2.6)$, for $\omega = 0.025$ and for two modes. Dashed lines correspond to the parallel base flow, straight lines to the actual DNS base flow.

6.2. *Numerical results*

The Newton–Raphson method has been applied successfully for both "even v" and "odd v" cases, but we will now present only results for the "even v" case, since it is the only case in which DNS-computed perturbations have been computed. These perturbations are generated by the interaction of a 2D TS-wave with the roughness elements. As explained in Section 2, the TS-wave amplitude is fixed so that the maximum value in y of the streamwise velocity component equals $10^{-4}U_\infty$ and the TS-wave circular frequency is $\omega = 7.91U_\infty/L_x = 0.025U_\infty/L$ [37]. This frequency has been chosen so that the roughness streamwise position (which corresponds here to $Re_{\delta_1} = 855$) is close to the first branch of the neutral stability curve (for two-dimensional perturbations).

Fig. 11 shows the streamwise evolution of the real and imaginary parts of α, for the β_0 and β_1 modes. This figure shows also the amplitude of the modes, which is defined as the integrated amplification between a given location X_0 and a location X:

$$A(X, X_0) = \exp\left(-\int_{X_0}^{X} \alpha_i(\xi)\,\mathrm{d}\xi\right). \tag{13}$$

The X values are scaled with L_x, and are thus the same as the ones plotted in Fig. 3. The streamwise wavenumbers and amplitudes computed for the parallel case are plotted as dash-dotted lines. We can observe that the real part of α (which is related to the instability wave phase speed) does not change significantly between the parallel and the pre-streaky case. On the contrary, the modes amplification is dissimilar: the pre-streaky modes reach much lower amplitudes than the parallel ones, showing a stabilizing effect of the pre-streaky structures. Whereas in the parallel case both modes are amplifying with X ($\alpha_i < 0$), and the most unstable mode is β_0, in the pre-streaky base flow case the most unstable mode is β_1. The β_0 mode is damped, except for $X \leqslant 2.65$, but this prediction must be considered carefully. Indeed, these streamwise locations are in the close vicinity of the roughness, in a region where the base

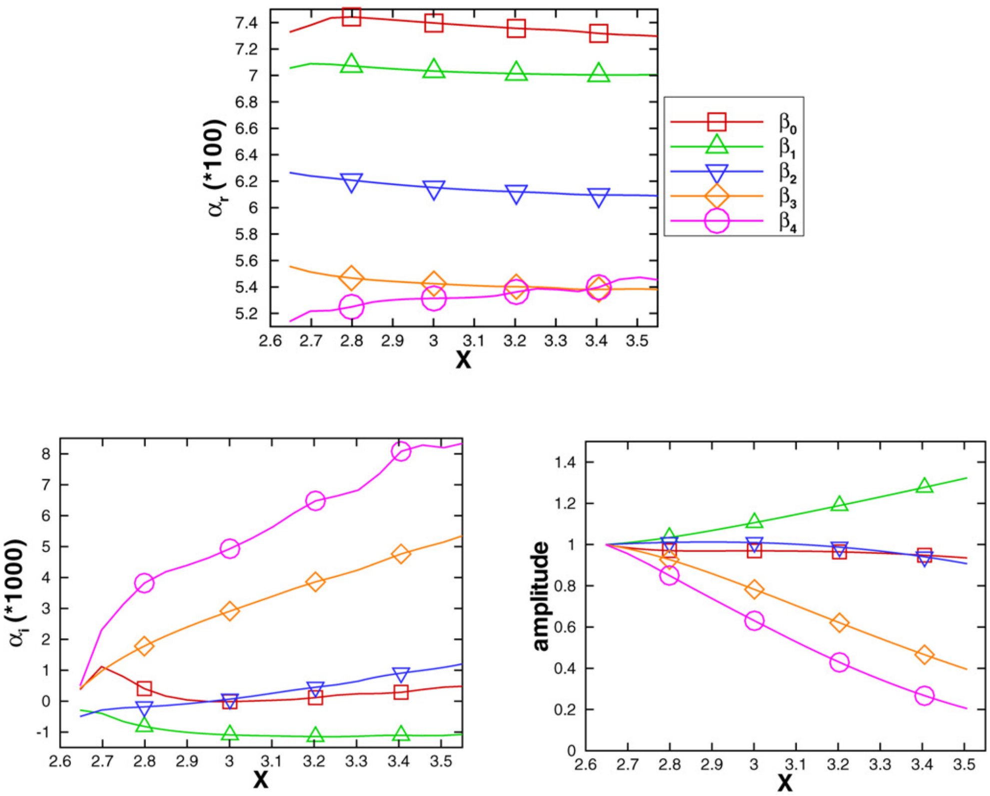

Fig. 12. Streamwise evolution of α and of the amplitude $A(X, 2.65)$, for $\omega = 0.025$ and for the first five modes.

flow may evolve quickly in X, which would invalidate the parallel assumption of "frozen in X" flow. Using a form in $\exp(\mathrm{i}\alpha x)$ for the perturbations could then be inadequate.

The streamwise evolution has also been computed for other modes, up to the β_4 mode. Higher modes computation requires a very fine discretization in the z direction, which has not been possible. Fig. 12 shows that for each mode the phase speed (proportional to $1/\alpha_r$) is almost constant with X, but that various modes have distinct phase speed values. Only the β_1 mode is amplifying with X, the other modes are almost always damped.

In practice, the receptivity process converts the forcing TS-wave into all the eigenmodes. However, far from the receptivity region, only the most amplified mode (associated to the lowest negative value of α_i) can be physically observed, since its resulting amplitude is much higher than the amplitudes of the other modes. In the present study, this should imply that the physical perturbation (which is the one reproduced in the DNS computations) is the β_1 mode. However, this is not the case, the β_1 eigenfunction being very different from the DNS-computed fluctuation. But since, as shown in Fig. 12, the α_i values are actually weak for all β_n modes, and since the studied X interval is small, the selection process of the most amplified mode may not have the time to be completely effective : the highest amplification ratio reached by the β_1 mode is only equal to 1.3. Therefore, the physical fluctuation should still be a linear combination of all the eigenmodes. This hypothesis will be checked in the next section.

7. Comparison between DNS-computed perturbation and biglobal eigenfunctions

7.1. The combination process

The DNS-computed perturbation is supposed to be a linear combination of all the β_n modes. The linear combination thus reads as:

$$q_{\mathrm{DNS}}(X, y, z) = \sum_n C_n q_n(X, y, z) \exp\left(\mathrm{i} \int_{x_0}^{x} \alpha_n \,\mathrm{d}\xi\right) \tag{14}$$

where q stands for the velocity perturbation $[u, v, w]$ and the C_n are complex coefficients. It must be noted that the streamwise location x is here scaled with L, the length scale also used in the y and z directions, in contrast to the 'frozen' streamwise location X, which is scaled by $L_x = L\sqrt{10^5}$.

The C_n coefficients are calculated at the streamwise location $X_0 = 3$ by using a least squares method, which minimizes the discrepancy between the DNS perturbation and the biglobal combination for all mesh points in the crossplane (y, z). First of all, the biglobal eigenfunctions q_n are normalized to their spatial maxima. Then, the C_n coefficients are the solution in the least squares sense to the system of equations:

$$2N_y \times N_z \left\{ \overbrace{\begin{bmatrix} v_0 & & v_N \\ & \cdots & \\ w_0 & & w_N \end{bmatrix}}^{N+1} \right. \begin{bmatrix} C_0 \\ \vdots \\ C_N \end{bmatrix} = \left. \overbrace{\begin{bmatrix} v_{\mathrm{DNS}} \\ w_{\mathrm{DNS}} \end{bmatrix}}^{1} \right\} 2N_y \times N_z. \tag{15}$$

In the present case, $N = 4$: only the β_0 to β_4 modes are taken into account in the combination. We have thus 5 unknown coefficients for $2N_y \times N_z$ relations. Next, the biglobal combination, denoted as q_{big}, is defined by:

$$q_{\mathrm{big}}(X_0 = 3, y, z) = \sum_{n=0}^{N} C_n q_n(X_0, y, z). \tag{16}$$

Finally, the biglobal combination is obtained at all the streamwise locations:

$$q_{\mathrm{big}}(X, y, z) = \sum_{n=0}^{N} C_n q_n(X, y, z) \exp\left(\mathrm{i} \int_{x_0}^{x} \alpha_n \, \mathrm{d}\xi \right) \tag{17}$$

where $x_0 = X_0 \cdot L/L_x = 3L/L_x$. As the combination process is performed with complex values, it must be noted that both the perturbation amplitude and phase are taken into account.

The whole process of comparison between the DNS and the stability results can be summarized as follows:

- the biglobal stability analysis is applied on the DNS steady base flow to compute the β_n modes;
- at each X location, each mode is normalized so that the complex streamwise velocity component is equal to unity at the spatial location (y, z) where its amplitude is maximal;
- a least squares method is performed at $X = 3$ to compute the C_n coefficients;
- the final biglobal combination solution is computed at all X locations using relation (17).

7.2. Results

In the present case, the values of the C_n coefficients are:

$$\begin{bmatrix} C_0 \\ C_1 \\ C_2 \\ C_3 \\ C_4 \end{bmatrix} = \begin{bmatrix} -44.15 + 28.93\mathrm{i} \\ 10.67 - 16.17\mathrm{i} \\ -3.34 - 1.55\mathrm{i} \\ -1.72 - 1.46\mathrm{i} \\ 35.87 + 8.15\mathrm{i} \end{bmatrix} \times 10^{-4}.$$

We can see that the coefficients values are decreasing with the n value, except for the C_4 coefficient. The latter is strong because it takes into account all the effects of the modal truncation.

Fig. 13 shows the comparison between $q_{\mathrm{DNS}}(X = 3, y, z)$ and $q_{\mathrm{big}}(X = 3, y, z)$. The left column corresponds to the real part of the perturbation velocities, the right column to the imaginary part. In this section, only the perturbations of the "even v" case have been computed. Therefore u and v are symmetric about $z = 0$, while w is antisymmetric. Each subfigure of Fig. 13 thus compares q_{DNS} for $z \leqslant 0$ with q_{big} for $z \geqslant 0$, except for the row corresponding to w, where w_{DNS} is compared to $-w_{\mathrm{big}}$. The agreement is excellent, especially for the v and w components. The differences observed on the u component may be due to some residual acoustics in the DNS computation. That is why only the v and w components of the velocity have been used to compute the C_n coefficients, as shown in Eq. (15). This

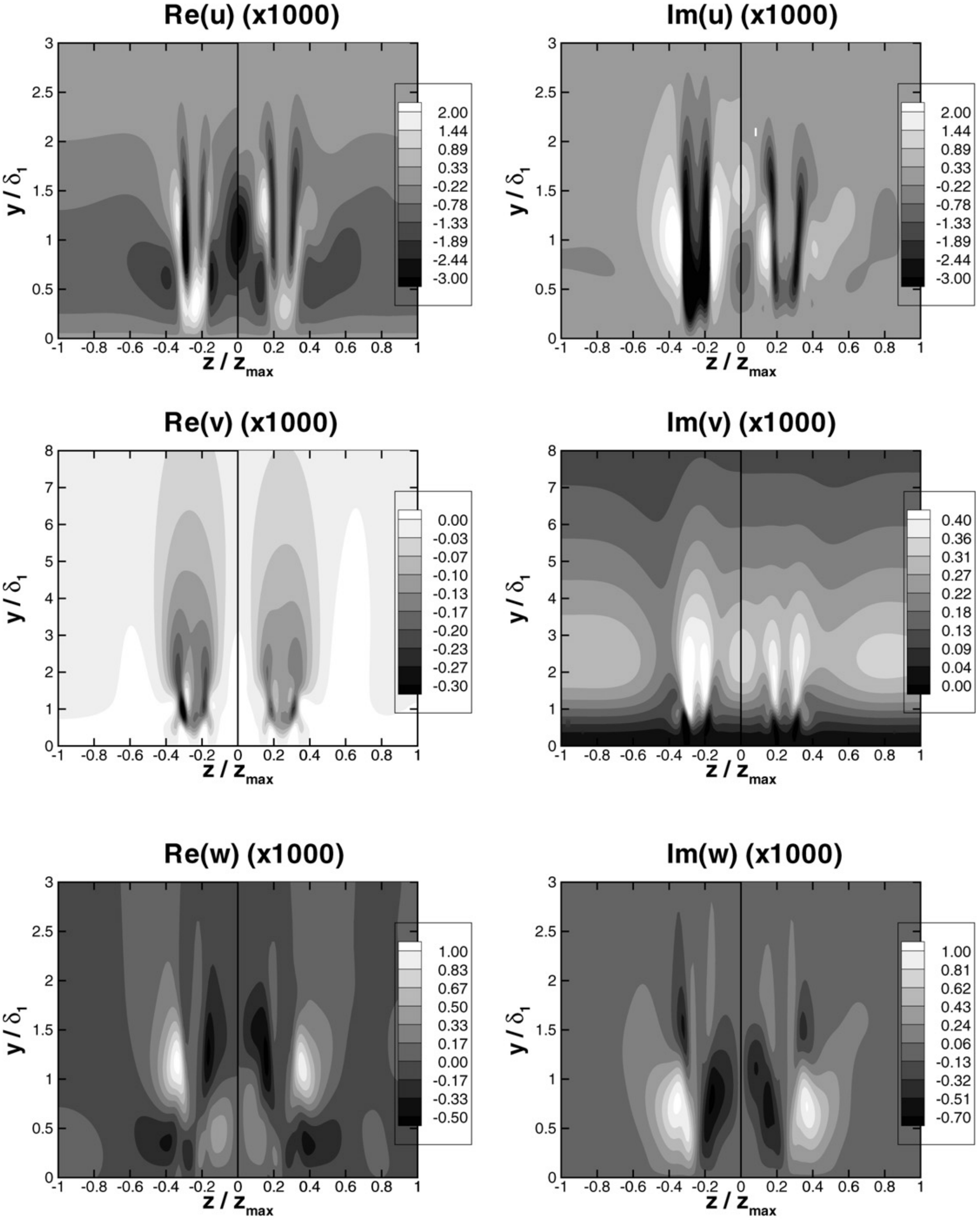

Fig. 13. Comparison between the DNS-computed perturbation (left-hand part of each figure, i.e. $z \leqslant 0$) and the perturbation obtained by the combination of the biglobal modes (right-hand part of each figure, i.e. $z \geqslant 0$). The streamwise location is $X = 3$. It has to be pointed out that the amplitude levels differ between the figures. As w is an odd function in z, the negative value of $Re(w)$ and $\mathrm{Im}(w)$ has been plotted for the biglobal modes combination.

is the choice which gives the best agreement. We can also see on Fig. 13 that the v velocity component reaches further out from the plate compared to the two others components. Finally, apart from the slight disagreement on the u component, this result shows that the DNS perturbations are a combination of the base flow eigenfunctions. Indeed,

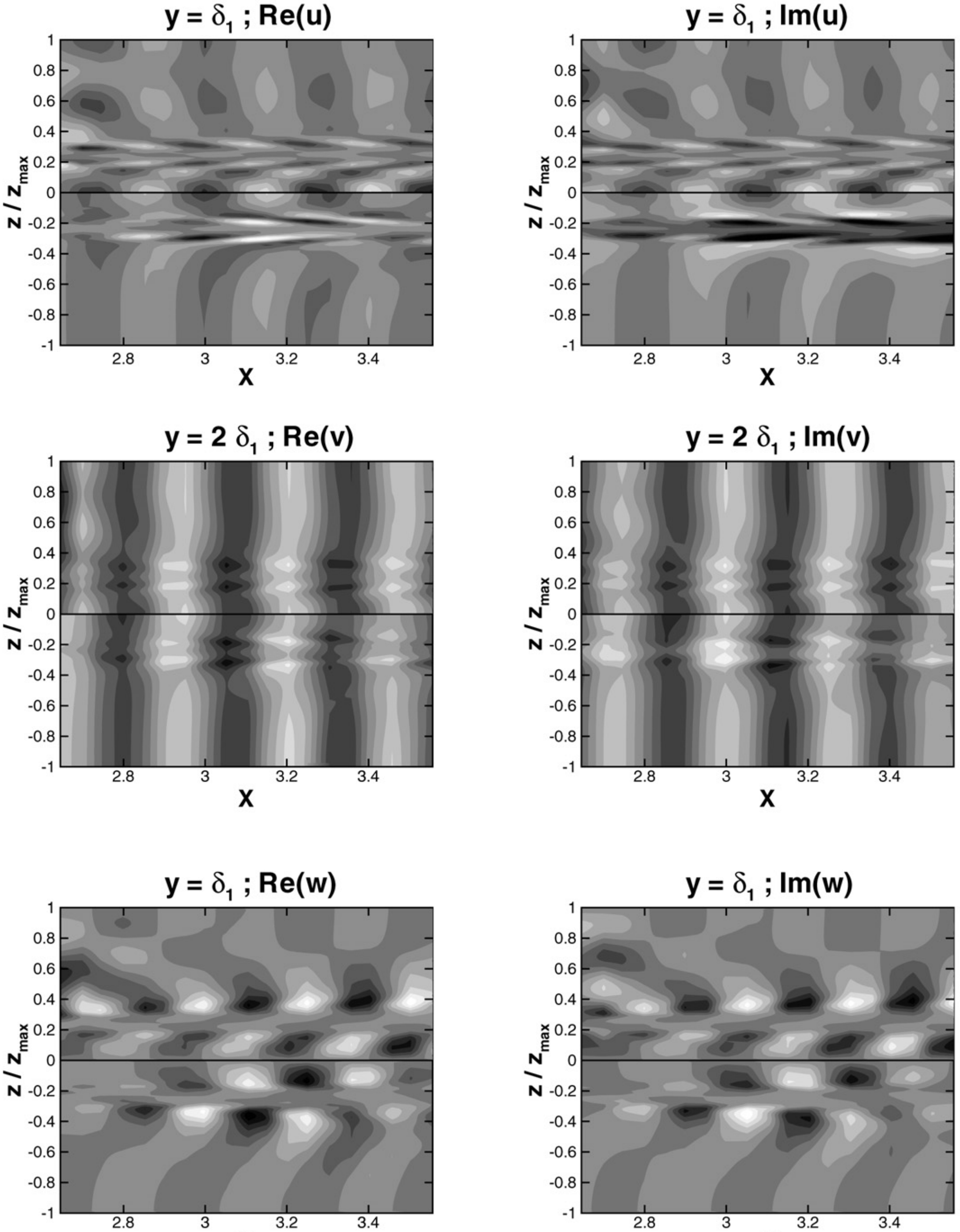

Fig. 14. Streamwise evolution of the DNS-computed perturbation (bottom part of each figure, i.e. $z \leqslant 0$) and of the perturbation obtained by the combination of the biglobal modes (top part of each figure, i.e. $z \geqslant 0$). The levels values are -5×10^{-3} to 5×10^{-3} in steps of 10^{-3} for the u-component, -5×10^{-4} to 5×10^{-4} in steps of 10^{-4} for the v-component and -1×10^{-3} to 1×10^{-3} in steps of 2×10^{-4} for the w-component. As w is an odd function in z, the negative value of $\mathrm{Re}(w)$ and $\mathrm{Im}(w)$ has been plotted for the biglobal modes combination.

even with only a few modes in the combination, the spatial evolution (y, z) and the respective amplitude of the various velocity components are correctly predicted.

As explained in Section 7.1, the biglobal combination has also been computed for other streamwise locations. As shown by Eq. (17), this has been done without recomputing the C_n coefficients, but by directly multiplying them by the exponential term associated to each mode. Results are shown in Fig. 14, in a presentation similar to the one used for Fig. 13, except that (X, z) planes are plotted rather than (y, z) planes. The chosen y values roughly correspond to the wall-normal locations of the maximum of each velocity component. That is why the y value for the v plots is twice as large as the one for the other plots. The results are once again very satisfactory, especially for the v and w components. The streamwise wave length is correctly predicted by the biglobal combination, and is between $0.25L_x$ and $0.28L_x$. Fig. 12 gives a streamwise wave length of the β_0 mode of $\lambda_0 \approx 0.27L_x$ while for the β_1 mode $\lambda_1 \approx 0.28L_x$. The higher modes have larger wavelengths. The biglobal combination wavelength does not then follow a specific mode's wavelength, but evolves as the DNS one. We can also see in Fig. 13 that the biglobal combination reproduces very well the complicated spatial evolution in the cross sections. However, the comparison is less good for $X < 2.85$ and $X > 3.3$. This is probably due to two different reasons: for $X < 2.85$, the parallel "frozen X" assumption, which implies the choice of a normal mode form in the streamwise direction, may be questionable, because of the closeness of the roughness location ($X_R = 2.471$). Apart from this, the combination process applied at $X < 2.85$ locations shows that the C_n coefficients change with X and that the obtained combination does not compare well with the DNS perturbation. Thus, either the eigenmodes are not a solution of the stability problem in this region or their respective amplitudes are not yet established. In this region, the DNS perturbation is certainly a more realistic representation than the biglobal one. On the contrary, for $X > 3.3$, the DNS solution is not completely converged, which could explain the differences to the biglobal solution.

8. Investigation of other frequencies

The results presented in the previous sections have been obtained for the frequency $\omega = 0.025$, which corresponds to $F = 79$ when the frequency is made dimensionless with $10^6 2\pi\nu/U_\infty^2$. As explained before, at the roughness location this frequency is near the lower branch of the neutral curve for the TS waves in the Blasius flow. In order to investigate the influence of the frequency on the stabilizing effect observed in 6 for $\omega = 0.025$, biglobal stability computations have been performed for other frequencies, from $\omega = 0.01$ to $\omega = 0.04$ (which is near the upper branch of the neutral curve). The results are presented in Fig. 15. The streamwise evolution of the amplitude $A(X, 2.8)$ (as defined in Eq. (13)) is plotted for the varicose β_0 and β_1 modes and for the sinuous β_1 mode. The varicose modes correspond to the "even v" case and the sinuous ones to the "odd v" case (see Section 4). The amplitudes obtained when the base flow is the pre-streaky flow are compared to those obtained in the Blasius flow case. The pre-streaky amplitudes are lower than the Blasius ones, whatever the considered modes or frequencies. The stabilizing effect is more important for the β_0 varicose and β_1 sinuous modes than for the β_1 varicose mode. Finally, the latter is the most amplified one in the pre-streaky case. This has already been observed for $\omega = 0.025$ in Section 6, and thus is still true for other frequencies. The sinuous mode, which has not been considered in the previous sections, undergoes an amplification very similar to the one of the β_0 varicose mode, whatever the base flow.

A close look at Fig. 15 shows that the higher the frequency, the stronger the stabilization. This effect is shown more clearly by Fig. 16. The values of α_i (i.e. the opposite of the spatial growth rate) for the β_0 varicose mode are plotted versus ω and X. In the Blasius case, for most of the plotted frequencies the mode is unstable, whereas in the pre-streaky case the mode is stable for all the frequencies. Moreover, the pre-streaky mode is much more stabilized for the highest frequencies than for the lowest ones. This could be related to the streamwise wavelength of the mode, which decreases with the frequency. Indeed, the phase speed of the β_0 varicose mode is between $0.28U_\infty$ for $\omega = 0.01$ and $0.38U_\infty$ for $\omega = 0.04$. As shown previously in Section 6 for $\omega = 0.025$, this phase speed is almost constant with X. The streamwise wavelength of the mode is thus $0.56L_x$ for $\omega = 0.01$ and $0.19L_x$ for $\omega = 0.04$. This could explain why the low-frequency modes are less sensitive to the presence of the pre-streaky distortions of the base flow. It must be pointed out that the phase speed is almost the same in the pre-streaky and Blasius flow cases, and that it is also true for the other modes. The phase speed of the β_1 varicose as well as the β_1 sinuous mode is about $0.36U_\infty$.

All these results show that the stabilizing effect of the pre-streaky structure observed in the previous sections for $\omega = 0.025$ can also be observed for other frequencies. Moreover the stabilization increases with the frequency. Finally, $\omega = 0.025$ is very close to the frequency for which the pre-streaky modes are the more amplified or the less damped.

9. Conclusions

The results of the present study can be summarized briefly in the following way. The steady pre-streaky flow generated by a roughness array placed in a Blasius boundary layer has been computed by a Direct Numerical Simulation.

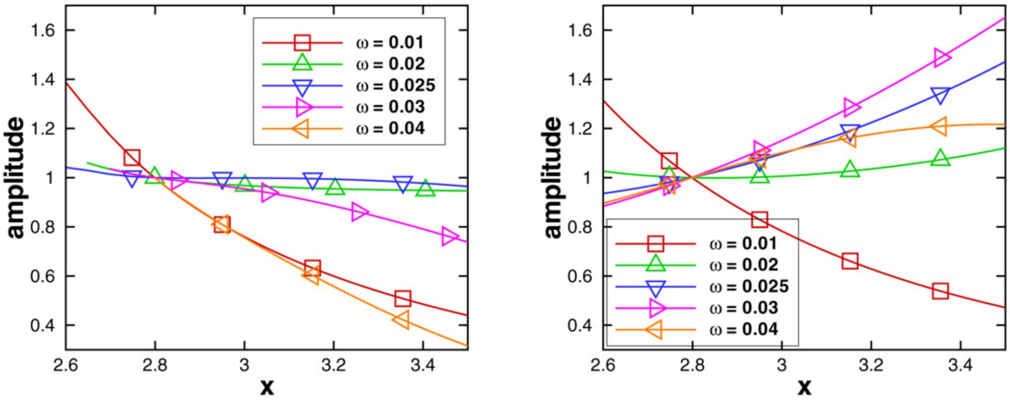

(a) β_0 varicose mode; Pre-streaky flow (b) β_0 varicose mode; Blasius flow

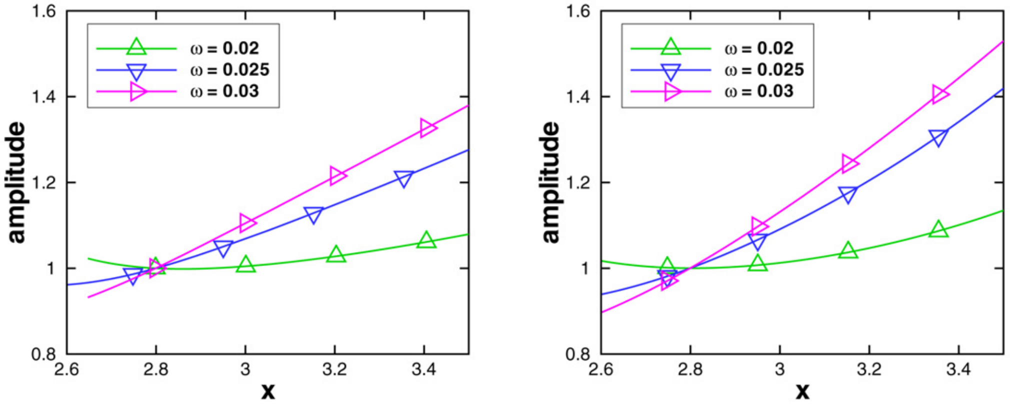

(c) β_1 varicose mode; Pre-streaky flow (d) β_1 varicose mode; Blasius flow

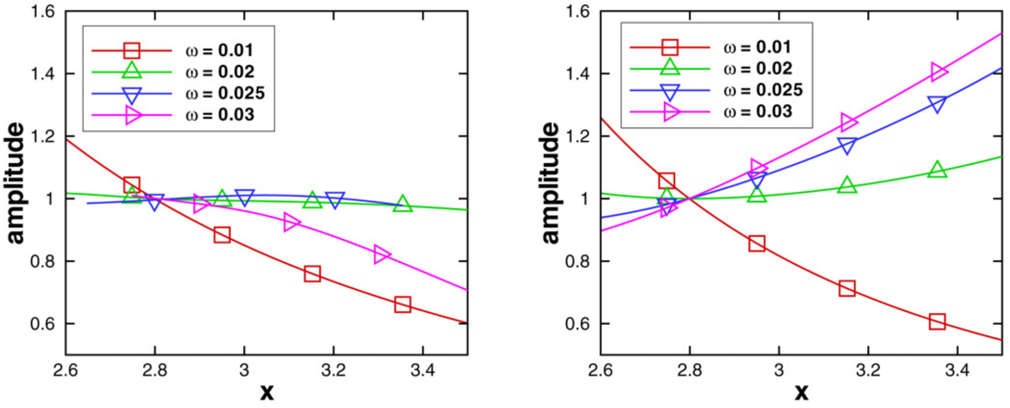

(e) β_1 sinuous mode; Pre-streaky flow (f) β_1 sinuous mode; Blasius flow

Fig. 15. Streamwise evolution of the amplitude $A(X, 2.8)$ for different frequencies. The right-hand side figures correspond to the stability modes of the Blasius flow, the left-hand side figures to the stability modes of the pre-streaky flow.

This flow has been used as a base flow for a biglobal linear stability study performed at each streamwise location. The stability analysis has shown that the eigenmodes of the pre-streaky flow are a continuation of the TS-waves associated with the unperturbed Blasius boundary layer flow. In particular their spanwise shape, which is sinusoidal for the Blasius TS-waves, shows strong peaks in the region of the roughness-induced streamwise vortices. We have not found any modes which would be intrinsic to the pre-streaky flow, i.e. which would not derive from a Blasius TS-wave.

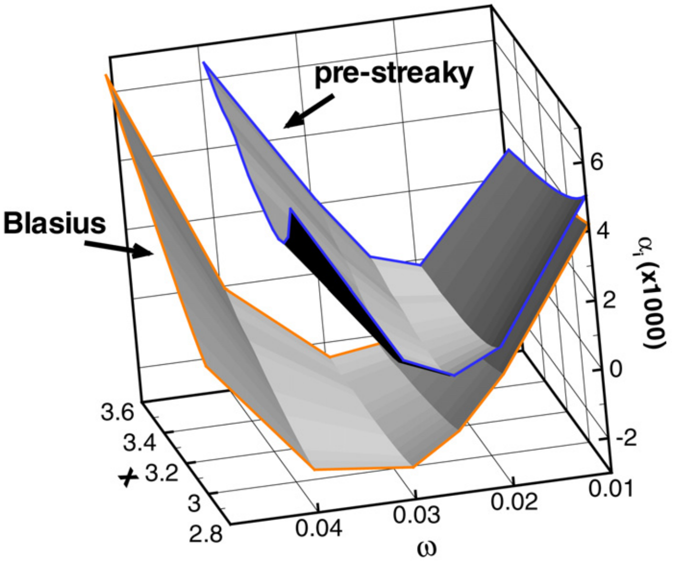

Fig. 16. Imaginary part of α versus the frequency and the streamwise location, for the β_0 varicose mode. Stability analysis performed on the pre-streaky flow and on the Blasius flow.

A spatial stability analysis has been performed for the frequency $\omega = 0.025U_\infty/L$, which corresponds to the lower branch of the Blasius neutral curve at the roughness location. This analysis has shown that the pre-streaky eigenmodes have the same streamwise wavelengths as the associated Blasius TS-waves, but smaller growth rates. There is thus a stabilizing effect of the steady roughness-induced vortices, in a similar way of what can be observed with steady streaks. Biglobal stability computations have also been performed for some other frequencies, up to the upper branch of the Blasius neutral curve. Whatever the frequency, the pre-streaky eigenmodes are much less amplified than the associated Blasius TS-waves. The stabilization process is more effective for the highest frequencies, which correspond to eigenmodes with the lowest streamwise wavelengths. The frequency $\omega = 0.025U_\infty/L$ is finally close to the one for which the eigenmodes are the most amplified.

A second Direct Numerical Simulation has been carried out, in which a two-dimensional TS-wave with frequency $\omega = 0.025U_\infty/L$ interacts with the roughness array and generates a highly oblique wave train downstream of the roughness elements. A least squares method has been used to find the linear combination of the pre-streaky eigenmodes which fits at best the DNS computed perturbation at a fixed streamwise location. The obtained coefficients are then used at the other streamwise positions, with a very good agreement except very close to the roughness element. This result gives us an explanation of what happens in the Direct Numerical Simulation. The incoming two-dimensional TS-wave interacts with the roughness elements; downstream, the scattering of the wave by the spanwise varying base flow generates the streaky eigenmodes. In the close vicinity of the roughness, the observable perturbation is not a linear combination of the eigenmodes, since either the generation process is not over or/and the parallel flow assumption used for computing the eigenmodes is not justified. Further downstream, the amplitudes of the eigenmodes evolve as foreseen by the normal mode stability theory. The linear combination of the pre-streaky eigenmodes reproduces the wave train evolution.

The combined use of the Direct Numerical Simulations and of the biglobal stability theory is thus useful to understand the physics of the pre-streaky flow. The receptivity process considered here as the interaction of a two-dimensional TS-wave with a roughness array ends very rapidly downstream of the roughness element. The generated instabilities are then clearly established. These phenomena occur in a region where the base flow can still be seen as a pre-streaky flow, the latter being a transient structure upstream of the usual streaky flow.

References

[1] I. Tani, H. Komoda, Y. Komatsu, M. Iuchi, Boundary-layer transition by isolated roughness, Tech. Rep. 375, Aeronautical Research Institute, University of Tokyo, November 1962.

[2] M. Acalar, C. Smith, A study of hairpin vortices in a laminar boundary layer: part 1, hairpin vortices generated by a hemisphere protuberance, J. Fluid Mech. 175 (1987) 1–41.

[3] H. Tufo, P. Fischer, M. Papka, K. Blom, Numerical simulation and immersive visualization of hairpin vortices, in: Proc. of the ACM/IEEE SC99 Conf. on High Performance Networking and Computing, IEEE Computer Soc., CDROM, 1999.

[4] B. Matheis, A. Rothmayer, Impact of surface roughness on local aerodynamics using a three-dimensional Navier–Stokes solver, in: AIAA 2004-0058, 42nd AIAA Aerospace Sciences Meeting and Exhibit, Reno, NV, 2004.

[5] V.V. Bogolepov, General scheme of three-dimensional local flows regimes, Z. Prikl. Mekh. Tekh. Fiz. 6 (1986) 80–91.

[6] I.I. Lipatov, I.V. Vinogradov, Three-dimensional flow near surface distortions for the compensation regime, Philos. Trans. R. Soc. London A 358 (2000) 3143–3153.

[7] M.T. Landahl, A note on algebraic instability of inviscid parallel shear flows, J. Fluid Mech. 98 (1980) 243.

[8] E. Reshotko, Transient growth: a factor in bypass transition, Phys. Fluids 13 (5) (2001) 1067–1075.

[9] P. Andersson, M. Berggren, D.S. Henningson, Optimal disturbances and bypass transition in boundary layers, Phys. Fluids 11 (1999) 134–150.

[10] P. Luchini, Reynolds-number-independent instability of the boundary layer over a flat surface: optimal perturbations, J. Fluid Mech. 404 (2000) 289–309.

[11] R.D. Joslin, C.E. Grosch, Growth characteristics downstream of a shallow bump: Computation and experiment, Phys. Fluids 7 (12) (1995) 3042–3047.

[12] M. Gaster, C.E. Grosch, T.L. Jackson, The velocity field created by a shallow bump in a boundary layer, Phys. Fluids 6 (9) (1994) 3079–3085.

[13] A. Tumin, E. Reshotko, Receptivity of a boundary-layer flow to a three-dimensional hump at finite Reynolds numbers, Phys. Fluids 17 (9) (2005) 094101 1–8.

[14] A. Tumin, E. Reshotko, The problem of boundary-layer flow encountering a three-dimensional hump revisited, in: AIAA-2004-101, 42nd AIAA Aerospace Sciences Meeting and Exhibit, Reno, NV, 2004.

[15] E.B. White, F.G. Ergin, Receptivity and transient growth of roughness-induced disturbances, in: AIAA-2003-4243, 33rd AIAA Fluids Dynamics Conference, Orlando, FL, 2003.

[16] E.B. White, J.M. Rice, F.G. Ergin, Receptivity of stationary transient disturbances to surface roughness, Phys. Fluids 17 (6) (2005) 064109 1–12.

[17] J.H.M. Fransson, L. Brandt, A. Talamelli, C. Cossu, Experimental and theoretical investigation of the nonmodal growth of steady streaks in a flat plate boundary layer, Phys. Fluids 16 (10) (2004) 3627–3638.

[18] P. Fischer, M. Choudhari, Numerical simulation of roughness-induced transient growth in a laminar boundary layer, in: AIAA-2004-2539, 34th AIAA Fluid Dynamics Conference and Exhibit, Portland, OR, 2004.

[19] M. Choudhari, P. Fischer, Roughness-induced transient growth, in: AIAA-2005-4765, 35th AIAA Fluid Dynamics Conference and Exhibit, Toronto, Ontario Canada, 2005.

[20] C. Cossu, L. Brandt, On Tollmien–Schlichting-like waves in streaky boundary layers, Eur. J. Mech. B Fluids 23 (2004) 815–833.

[21] M.N. Kogan, M.V. Ustinov, Boundary layer stabilization by artificial turbulence, Fluid Dynamics 38 (4) (2003) 571–580.

[22] J.H.M. Fransson, L. Brandt, A. Talamelli, C. Cossu, Experimental study of the stabilization of Tollmien–Schlichting waves by finite amplitude streaks, Phys. Fluids 17 (5) (2005) 054110, 1–15.

[23] J.H.M. Fransson, A. Talamelli, L. Brandt, C. Cossu, Experimental analysis of transition delay by means of roughness elements, in: AIAA-2006-3528, 36th AIAA Fluids Dynamics Conference and Exhibit, San Francisco, CA, 2006.

[24] J.H.M. Fransson, A. Talamelli, L. Brandt, C. Cossu, Delaying transition to turbulence by a passive mechanism, Phys. Rev. Lett. 96 (6) (2006) 064501 1–4.

[25] V. Theofilis, Advances in global linear instability analysis of nonparallel and three-dimensional flows, Progr. Aerospace Sci. 39 (2003) 249–315.

[26] U. Rist, H. Fasel, Direct numerical simulation of controlled transition in a flat-plate boundary layer, J. Fluid Mech. 298 (1995) 211–248.

[27] C.S. Peskin, Numerical analysis of blood flow in the heart, J. Comput. Phys. 25 (3) (1977) 220–252.

[28] D. Goldstein, R. Handler, L. Sirovich, Modeling a no-slip flow boundary with an external force field, J. Comput. Phys. 105 (2) (1993) 354–366.

[29] M. Linnick, Investigation of actuators for use in active flow control, Master's thesis, Dept. of Aerospace and Mechanical Engineering, Univ. of Arizona, Tucson, AZ, 1999.

[30] D.A. von Terzi, M.N. Linnick, J. Seidel, H. Fasel, Immersed boundary techniques for high-order finite-difference methods, in: AIAA 2001-2918, 31st AIAA Fluids Dynamics Conference, 2001.

[31] W. Würz, S. Herr, A. Wörner, U. Rist, S. Wagner, Y.S. Kachanov, Three-dimensional acoustic-roughness receptivity of a boundary layer on an airfoil: experiment and direct numerical simulations, J. Fluid Mech. 478 (2003) 135–163.

[32] S.A. Orszag, Numerical simulation of incompressible flows within simple boundaries. I. Galerkin (spectral) representations, Stud. Appl. Math. L(4) (1971) 1.

[33] C. Davies, P. Carpenter, Numerical simulation of the evolution of Tollmien–Schlichting waves over finite compliant panels, J. Fluid Mech. 335 (1997) 361–392.

[34] M. Kloker, U. Konzelmann, H. Fasel, Outflow boundary conditions for spatial Navier–Stokes simulations of transitional boundary layers, AIAA J. 331 (4) (1993) 620–628.

[35] A. Wörner, U. Rist, S. Wagner, Humps/steps influence on stability characteristics of two-dimensional laminar boundary layer, AIAA J. 41 (2) (2003) 192–197.

[36] U. Maucher, U. Rist, S. Wagner, A method for the identification of high-frequency oscillations in unsteady flows, ZAMM, Z. Angew. Math. Mech. 77 (Suppl. 1) (1997) S209–S210.

[37] A. Wörner, Numerische Untersuchung zum Entstehungsprozess von Grenzschichstörungen durch die Interaktion von Schallwellen mit Oberflächenrauhigkeiten, Ph.D. thesis, Stuttgart University, 2003.

[38] C. Canuto, Y.M. Hussaini, A. Quarteroni, T.A. Zang, Spectral Methods in Fluid Dynamics, Springer, New York, 1988.
[39] G. Casalis, Méthodes mathématiques pour la mécanique, ENSAE Course, 2004.
[40] M.V. Ustinov, Stability of the flow in a streaky structure and the development of perturbations generated by a point source inside it, Fluid Dynam. 37 (1) (2002) 9–20.